Turbulence and transport in mirror geometries in the Large Plasma Device

Phil Travis [1],† and Troy Carter [1,2]

[1]Department of Physics and Astronomy, University of California, Los Angeles, CA 90095-1547, USA

[2]Oak Ridge National Laboratory, Oak Ridge, TN 37830, USA

Thanks to advances in plasma science and enabling technology, mirror machines are being reconsidered for fusion power plants and as possible fusion volumetric neutron sources. However, cross-field transport and turbulence in mirrors remains relatively understudied compared with toroidal devices. Turbulence and transport in mirror configurations were studied utilizing the flexible magnetic geometry of the Large Plasma Device (LAPD). Multiple mirror ratios from $M = 1$ to $M = 2.68$ and three mirror-cell lengths from $L = 3.51$ to $L = 10.86$ m were examined. Langmuir and magnetic probes were used to measure profiles of density, temperature, potential and magnetic field. The electric field-fluctuation-driven $\tilde{E} \times B$ particle flux, where B is the background field, was calculated from these quantities. Two probe correlation techniques were used to infer wavenumbers and two-dimensional structure. Cross-field particle flux and density fluctuation power decreased with increased mirror ratio. Core density and temperatures remain similar with mirror ratio, but radial line-integrated density increased. The physical expansion of the plasma in the mirror cell by using a higher field in the source region may have led to reduced density fluctuation power through the increased gradient scale length. This increased scale length reduced the growth rate and saturation level of rotational interchange and drift-like instabilities. Despite the introduction of magnetic curvature, no evidence of mirror-driven instabilities – interchange, velocity space or otherwise – were observed. For curvature-induced interchange, many possible stabilization mechanisms were present, suppressing the visibility of the instability.

Keywords: plasma confinement, plasma instabilities

1. Introduction

Historically, mirror research has prioritized the main issues with mirror confinement: stabilizing the interchange instability, stabilizing velocity-space (loss-cone-driven) instabilities and minimizing axial electron heat losses. Nevertheless, cross-field transport remains an important topic in magnetic-confinement fusion reactor development, in both linear and toroidal geometries. Insight into edge-relevant turbulence, and its coupling to

† Email address for correspondence: phil@physics.ucla.edu

interchange and other mirror-driven instabilities, performed in a basic plasma science device may be useful for a mirror-based reactor. Although not at fusion-relevant core temperatures or densities, the Large Plasma Device (LAPD) operates at conditions similar to the edge of fusion devices and can provide insight into the physical processes in that region. Mirror machines are once again rising in prominence as a candidate for commercial fusion reactors with the advent of highly funded commercial ventures and high-field high-temperature superconducting magnets (Endrizzi *et al.* 2023; Forest *et al.* 2024), so development of a functional understanding of cross-field transport in mirrors is imperative. A characterization of edge fluctuations has been undertaken, with emphasis on interpreting these fluctuations within the context of a mirror.

Non-classical cross-field particle transport is often caused by low-frequency, large-amplitude fluctuations. These fluctuations are the result of various instabilities. One such process is the 'universal' drift instability, which appears in the presence of a density gradient and finite resistivity. Drift-wave turbulence and the effect on transport has been extensively studied in the past (Horton 1999; Tynan, Fujisawa & McKee 2009). In the presence of sufficiently high rotation or sheared flow, rotational interchange and the Kelvin–Helmholtz instabilities also contribute or couple to these fluctuations.

Various gradient-, rotation- and shear-driven instabilities (and suppression of such) have been studied previously in the LAPD experimentally (Schaffner *et al.* 2012, 2013; Schaffner 2013) and in simulations using BOUT, a three-dimensional fluid turbulence code, and an eigenvalue solver (Popovich *et al.* 2010). The LAPD has a sufficiently high spontaneous rotation rate that rotation-driven instabilities may be excited without artificial drive. Simulations using BOUT++ (Friedman *et al.* 2013) have also suggested that a rapidly growing nonlinear instability may dominate over all other linear instabilities.

Imposing a magnetic mirror configuration introduces magnetic curvature. The alignment of the curvature vector with a pressure gradient vector component causes the flute-like interchange instability if no stabilization mechanism is present. This interchange mode could couple to finite parallel wavenumber, $k_\parallel$ drift waves. The coupling of drift waves to curvature-induced interchange modes has been studied in toroidal devices such as TORPEX (Fasoli *et al.* 2006; Poli *et al.* 2006), where curvature was seen as the driving component for the unstable drift-interchange modes. Drift-like fluctuations have also been observed in the GAMMA-10 mirror (Mase *et al.* 1991; Yoshikawa *et al.* 2010). Flute-like modes and drift waves have been studied in other linear devices, such as Mirabelle (Brochard, Gravier & Bonhomme 2005), where the appearance of flute-like modes or drift waves were controlled by varying the field and limiter diameter.

The rotational interchange and curvature interchange can both be flute-like modes. Rotational interchange (also called the 'centrifugal instability') is driven by the aligned centrifugal force and pressure gradient vectors, but curvature-driven interchange is instead driven by magnetic curvature and is typically referred to as simply the 'flute' or 'interchange' instability. Rotational interchange (Jassby 1972) has been observed in the LAPD in the past (Schaffner *et al.* 2012; Schaffner 2013), and the curvature-driven interchange instability has been observed in many other mirror machines (Wickham & Vandegrift 1982; Ferron *et al.* 1983; Post 1987).

Biasing or modifying the electrical connection of the plasma with the end wall has proven to be a important actuator in many mirror machines such as TMX-U (Hooper *et al.* 1984), GAMMA-10 (Mase *et al.* 1991) and GDT (Bagryansky *et al.* 2003; Bagryansky, Beklemishev & Soldatkina 2007; Beklemishev *et al.* 2010), and will be utilized on WHAM (Endrizzi *et al.* 2023). Active biasing was not attempted in this study, but the intrinsic rotation and strong electrical connection to the source region may provide a useful analogue for edge biasing in other mirror machines.

The LAPD exhibits a high degree of turbulence so it is difficult to identify the dispersion relation of the modes that are present. Nevertheless, the LAPD has good coverage of perpendicular spectra using correlation-plane techniques, and some measure of parallel spectra using the correlation between two axially separated probes. A space–time spectral characterization of the many instabilities present in this low beta (ratio of plasma pressure to magnetic pressure), moderate aspect ratio, gas-dynamic trap regime is attempted.

This goal of this study was to investigate the changes to turbulence and transport in LAPD mirror configurations. Of particular interest were the potential coupling of the interchange instability with drift waves or other modes, and the effect of the mirror geometry on cross-field particle flux. Presented is a characterization of the observed modes and the effect of introducing a mirror geometry. This paper is organized as follows. Section 2 discusses the configuration of the LAPD and the diagnostics used. Section 3 covers the changes seen when imposing a magnetic mirror configuration on profiles, particle flux, drift waves, turbulence and magnetic fluctuations. Section 4 explores the changes in two dimensions (x–y plane) structure. Section 5 discusses the active and expected instabilities and reasons for their modification. Section 6 summarizes the study and discusses the requirements for a deeper investigation.

2. Device configuration

2.1. *The Large Plasma Device*

The LAPD is a 20 m long, 1 m diameter basic plasma device at UCLA (Gekelman *et al.* 2016). The LAPD has a variable magnetic field, from 250 G to 1.6 kG and can be varied axially. Probes inserted into the plasma can collect high-resolution, temporal information on density, temperature, potential and magnetic field fluctuations. In this study, the plasma was formed using an emissive, 72 cm diameter barium-oxide (BaO) cathode (mapped to 60 cm in a flat field) and a 72 cm diameter, 50 % transparent molybdenum anode that accelerate electrons across a configurable 40–70 V potential; voltages of 60 and 63 V were used in this study. The source has since been upgraded to a lanthanum hexaboride (LaB6) cathode (Qian *et al.* 2023) that enables access to higher-density, higher-temperature regimes, but all the data in this study are from plasma formed by a BaO cathode.

The flexible magnetic geometry of the LAPD was used to construct a variety of magnetic mirror configurations. The discharge current, fill pressure and other machine parameters were held constant. The typical plasma parameters observed in this study can be seen in table 2. Data at several mirror ratios and lengths were collected (see table 1) but emphasis is placed on the short cell because the highest mirror ratio possible ($M = 2.68$) with a 500 Gauss midplane field could be accessed and probes were able to be placed outside of the mirror cell. An overview of the axial magnetic field for the short mirror configurations and probe locations can be seen in figure 1. The 2- or 3-cell mirror configurations were also explored but are not examined in this study. All results presented below are from the short mirror-cell configuration unless otherwise specified.

2.2. *Diagnostics*

All diagnostics were recorded with an effective sampling rate of 6.25 MHz (16-sample average at 100 Msps) and a spatial resolution of 0.5 cm. When necessary, averaging over time is done in the approximate steady-state period of the plasma discharge (4.8 to 11.2 ms from the 1 kA trigger signal). Unless otherwise noted, all data presented will be from probes inside the mirror region ($z \approx 7$ m). An example of a raw ion saturation current $- I_{sat} = 0.6 S n_e e \frac{\sqrt{T_e}}{m_i}$, where S is effective area, n_e electron density, e elementary charge, T_e electron temperature, and m_i ion mass – signal and processing steps can be seen in

Mirror length	Mirror ratios (M)			
Flat	1	—	—	—
3.51 m (short)	1.47	1.90	2.30	2.68
7.03 m (medium)	1.49	1.98	2.46	—
10.86 m (long)	1.47	1.97	2.44	—

TABLE 1. Magnetic mirror lengths and ratios. The lengths are measured where the curvature changes sign and the ratio is the maximum divided by the minimum. Approximately 3.5 m must be added to the length if the good-curvature region is included. In the case of small asymmetries, the field strengths were averaged before calculation of the mirror ratio.

Cathode radius ($M = 1$)	x_c	30		cm
Machine radius	R	50		cm
Plasma length	L	~ 17		m
Primary species	—	He-4 1+		—
Electron-helium mass ratio	—	1.37×10^{-4}		—
Neutral pressure		6–20×10^{-5}		Torr
Quantity		Core	$x = x_{PF}$	Unit
Density	n_e	1.25×10^{12}	0.6×10^{12}	cm^{-3}
Ion temperature	T_i	~ 1	—	eV
Electron temperature	T_e	4	5	eV
Beta (total)	β	9×10^{-4}	6×10^{-4}	—
Midplane magnetic field	B_{mid}	500	—	G
Plasma freq	Ω_{pe}	10	7.1	GHz
Ion cyclotron freq	Ω_{ci}	200	—	kHz
Electron cyclotron freq	Ω_{ce}	1.4	—	GHz
Debye length	λ_D	0.013	0.021	mm
Electron skin depth	λ_e	30	43	mm
Ion gyroradius	λ_{ci}	5.8	—	mm
Electron gyroradius	λ_{ce}	0.13	0.15	mm
Ion thermal velocity	$\bar{v}_i$	6.94	—	km s^{-1}
Electron thermal velocity	$\bar{v}_e$	1190	1330	km s^{-1}
Sound speed	c_s	13.0	13.9	km s^{-1}
Alfvén speed	v_a	446–1140	-1620	km s^{-1}
Ion sound radius	ρ_s	65	69	mm
Ion-ion collision freq	ν_{ii}	730	380	kHz
Electron-ion collision freq	ν_{ei}	6.77	2.59	MHz
Electron collision freq	ν_{ee}	9.57	3.66	MHz
Ion mean free path	$\lambda_{i,mfp}$	26	50	mm
Electron mean free path	$\lambda_{e,mfp}$	175	512	mm
Spitzer resistivity	η	192	146	$\mu\Omega$m

TABLE 2. The LAPD machine information and plasma parameters in the core and peak-fluctuation region ($x = x_{PF}$) at the midplane in this study. Dashed quantities are assumed to be identical to core quantities.
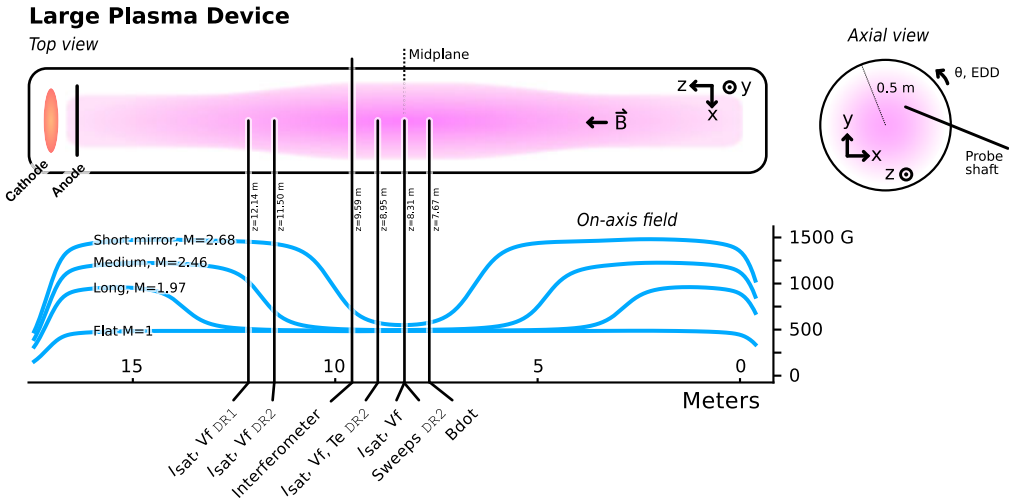
FIGURE 1. Cartoon of the LAPD and the coordinate system used. Only four of the eleven mirror configurations studied are plotted for clarity (mirrors of the same length have similar shapes and simply scale with mirror ratio). Diagnostic set varied by datarun; unlabelled diagnostics were used in both dataruns.
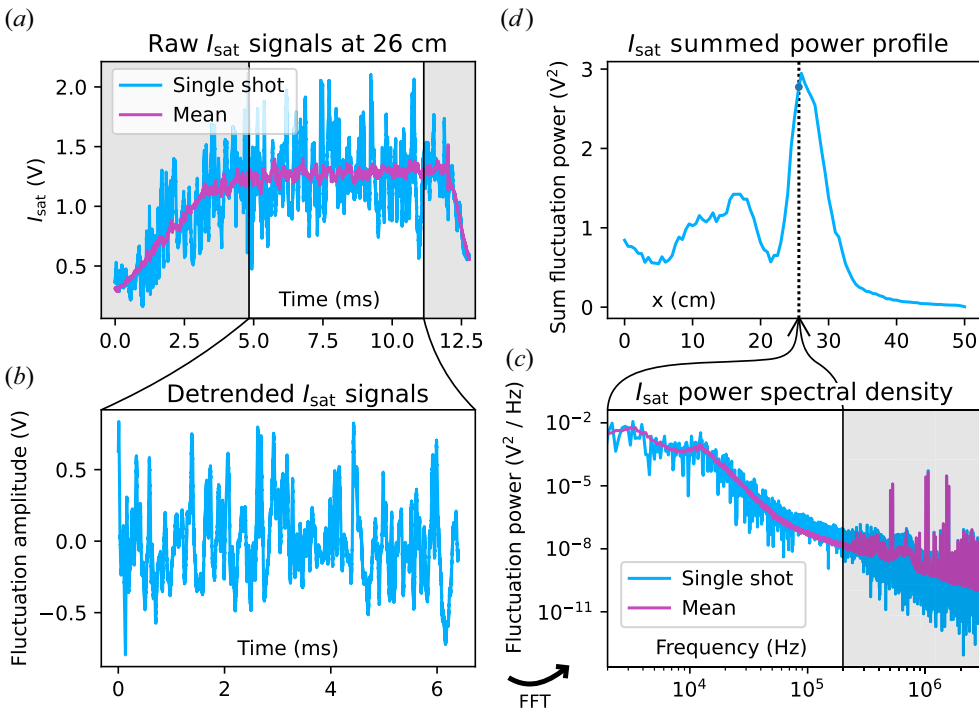

FIGURE 2. Raw data and basic processing steps for LAPD probe diagnostics as demonstrated by an I_{sat} trace from a DR1, $M = 1$ mirror at 26 cm. Data are truncated from 4.8 to 11.2 ms (*a*) and detrended (*b*). Power spectral density is calculated (*c*), and a power profiles can be constructed (*d*). The shaded regions are excluded from this analysis.

figure 2. The raw signals are detrended by subtracting the mean across shots to obtain the fluctuations only. Fast Fourier transformations are then taken of these fluctuations for calculating power spectra and cross-correlated quantities. Frequencies above 200 kHz are dominated by electronics and instrumentation noise and thus are also ignored. Fluctuation power profiles can then be constructed.

The data presented were collected in two phases. The first phase ('datarun'), DR1, collected Langmuir probe (I_{sat} and Vf – floating potential) and magnetic fluctuation ('Bdot') (Everson *et al.* 2009) traces. Fifty shots were taken at each position for every configuration. The second phase, DR2, was conducted with a similar set of diagnostics focused on temperature measurements (swept and triple probe) and the two-dimensional x–y structure. Fifteen shots were taken at each position, except for Langmuir sweeps with 64 shots. When appropriate, all data for each position were shot averaged. The parameter 'I_{sat}' will be used interchangeably with 'density' and be presented with units of density (assuming a flat electron temperature $T_e = 4.5$ eV profile).

3. Mirror-induced changes

3.1. *Profile modification*

Because the field at the plasma source increases with M, the midplane plasma expands by a factor of $\sqrt{M}$. The physical locations of the peak-fluctuation region – x_{PF} (maximum gradient) – and the cathode radius x_c can be seen in table 3. This expansion leads to broader plasma profiles and decreased core density but these profiles are similar in the core and at x_{PF} when magnetically mapped to the cathode radius x_c, as seen in figure 3. Dips between the core ($x/x_c = 0$) and the peak-fluctuation region ($x = x_{PF}$) are seen, but fluctuation power from this region ($x/x_c = 0.5$ to 0.7) is not significant (figure 7) so this region is not the focus of this study. The line-integrated density as measured by a 56 GHz heterodyne interferometer increases up to $\sim 35\%$ from the $M = 1$ case of $\approx 8 \times 10^{13}$ cm^{-2} (figure 4) but does not increase past a mirror ratio of 2.3. Discharge power increases only slightly (3 %) at higher mirror ratios, suggesting negligible impact on density. Langmuir sweeps and triple probe measurements of T_e (DR2) show slightly (less than 25 %) depressed core and slightly elevated edge T_e with increasing mirror ratio (figure 5) but otherwise remains unaffected. The temperature affects I_{sat} measurements through the $\sqrt{T_e}$ term so small changes are insignificant. The low temperatures indicate that the plasma is collisional given the length scales of the system (as seen in table 2) and isotropic. Plasma potential decreases across the plasma (figure 6) when the mirror ratio exceeds 1.9. This drop in plasma potential may be caused by the grounding of the anode to the wall, which should begin at $M = 1.93$ given the 72 cm anode and 100 cm vessel diameters. The reason for the local minimum in the $M = 2.68$ is unknown. This potential profile creates a sheared $\boldsymbol{E} \times \boldsymbol{B}$ velocity profile (figure 6) limited to 500 m s^{-1} in the core and exceeding ~ 3 km s^{-1} at the far edge. The flow does not exceed 4 % of the sound speed (table 2) in the core or gradient ($x = x_{PF}$) region. The mirror ratio does not appear to significantly alter azimuthal flow. The floating potential (Vf) profile also exhibits similar behaviour to the plasma potential (figure 6), but is modified by the presence of primary electrons.

3.2. *Reduced particle flux*

The density fluctuation power peaks at the steepest gradient region ($x_{PF} = x/x_c \sim 0.88$) as expected, as seen in figure 7. Here, x_{PF} occurs at nearly the same magnetically mapped coordinate for each mirror ratio. These density fluctuations are a large driver of changes in the cross-field particle flux (3.1). The Vf fluctuations also peak at the same location, but the total power across mirror ratios is similar and, relative to density fluctuations, much

Mirror ratio	1	1.47	1.90	2.30	2.68
Scale factor	1	1.21	1.38	1.52	1.64
x_c (cm)	30	36	41	45	49
x_{PF} (cm)	26	32	36	40	43

TABLE 3. The x_c and x_{PF} locations for each mirror ratio when scaled by the expected magnetic expansion.
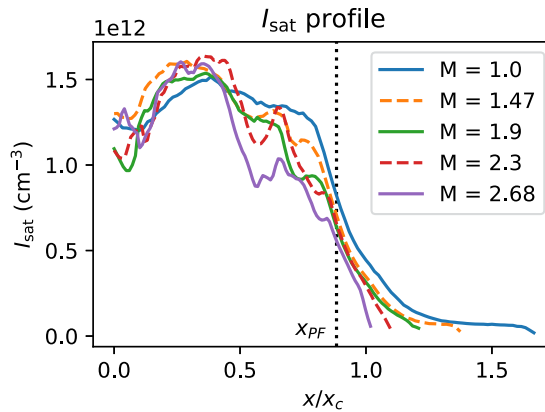

FIGURE 3. Midplane I_{sat} profile, shot averaged and time averaged from 4.8 to 11.2 ms (we have assumed $T_e = 4.5$ eV based on triple probe and Langmuir sweep measurements). Effective area was calibrated using a nearby interferometer. Profile shape remains similar in the core and gradient region when mapped to the cathode radius x_c. The dips in profiles at higher M below $x = x_{PF}$ are of unknown origin and are not the focus of this study. Shot-to-shot variation is less than 5 % for $x \leqslant 0.95x_c$ and less than 9 % for $x \leqslant 1.4x_c$ for all cases.
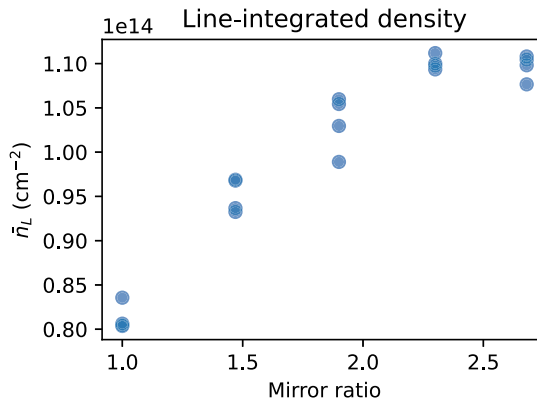
FIGURE 4. Line-integrated density as measured by a 56 GHz heterodyne interferometer as a function of mirror ratio, taken from four discharges for each mirror configuration. Density increases up to a mirror ratio of 2.3, where it appears to level off. The interferometer is located in the mirror-cell bad-curvature region at 9.59 m, 1.3 m closer to the cathode from the midplane.
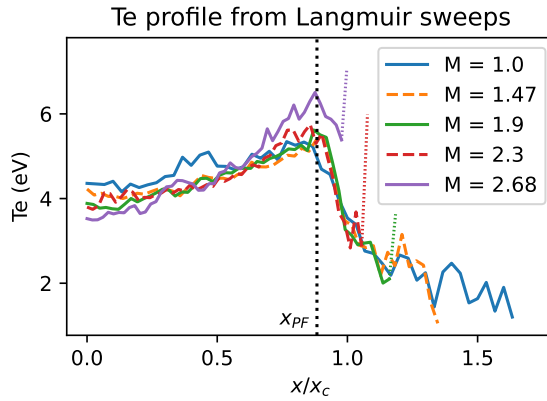
Te profile from Langmuir sweeps

FIGURE 5. The value of T_e from Langmuir sweeps (DR2) at the midplane. Triple probe results are nearly identical. The increased temperatures directly at the plasma edge, indicated by dotted portions of the curves, are likely artefacts caused by sheath expansion in lower densities. Changes in mirror ratio lead to at most a 25 % change in T_e. The plasma is collisional and isotropic.
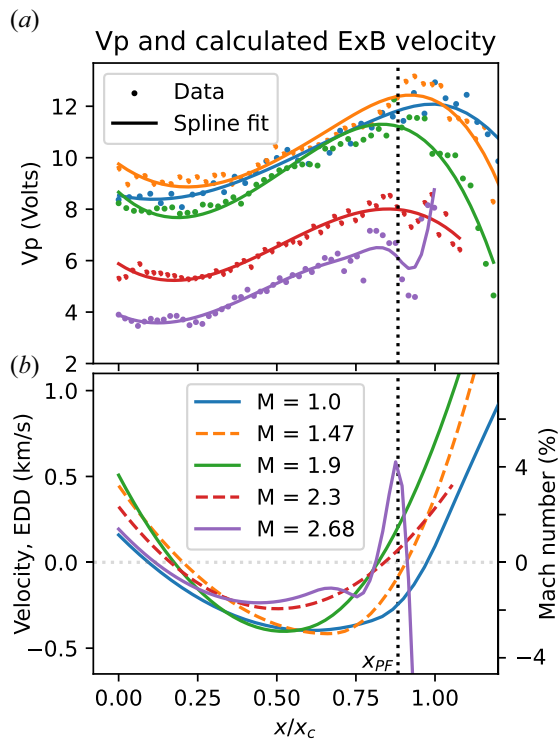

FIGURE 6. Plasma potential Vp (*a*) and derived ***E*** ✕ ***B*** velocity profiles (*b*) from Langmuir sweeps at the midplane. The range $x/x_c > 1.2$ has been excluded from the graph for greater clarity in the core and gradient region. The electric field was calculated by taking the gradient of the spline-smoothed plasma potential profile. The Mach number (in per cent) is calculated using the approximate sound speed evaluated at $x = x_{PF}$ (table 2). The overall structure of the flows does not appreciably change when mirror ratio is varied.
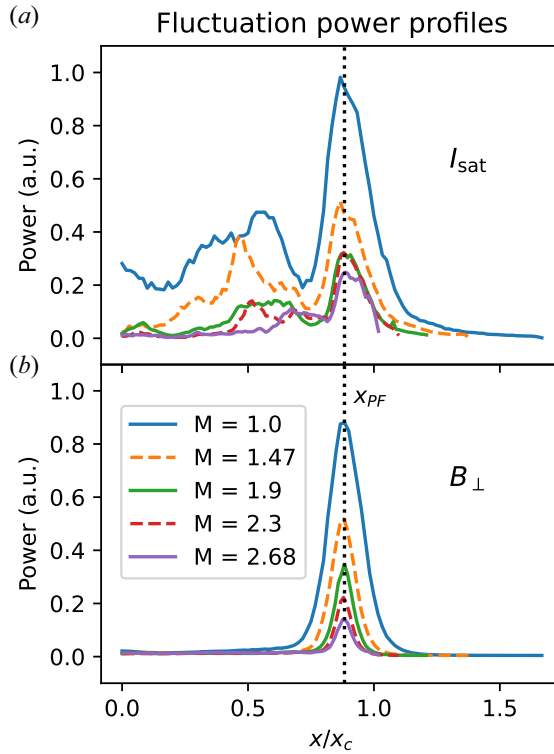
(a)

Fluctuation power profiles

FIGURE 7. The I_{sat} (a) and $B_\perp$ (b) fluctuation power profiles for signals 2 kHz and up at $z = 8.3$ m (midplane) and $z = 7.7$ m, respectively. The lower-frequency components in I_{sat} are associated with bulk profile evolution, dominate the core region and are not the focus of this study.

lower in the core. Core density fluctuations below 2 kHz are substantial in the core at lower mirror ratios, possibly caused by hollow profiles, non-uniform cathode emissivity or probe perturbations, but are outside the scope of this study.

A spectral decomposition technique is used to calculate the time-averaged particle flux (Powers 1974) as seen in figure 8

$$\Gamma_{\tilde{E}\times B} = \langle \tilde{n}\tilde{v} \rangle = \frac{2}{B} \int_0^\infty k\,(\omega)\,\gamma_{n\phi}\,(\omega)\sin\left(\alpha_{n\phi}\right)\sqrt{P_{\text{nn}}\,(\omega)\,P_{\phi\phi}\,(\omega)}\,\mathrm{d}\omega, \qquad (3.1)$$

where k is the azimuthal wavenumber component, γ is the coherency, α is the cross-phase, P is the power spectrum and ω is the frequency. This method is more robust than the naive time integration of $n(t)\tilde{E}(t)$ because it accounts for the coherency of the density–potential fluctuations. This representation also enables inspection of each contributing term in the event of surprising or problematic results. A plot of the I_{sat}-Vf phase can be seen in figure 9. The flattened particle flux in the core is likely caused by primary electrons emitted by the cathode. These electrons have long mean free paths (greater than a few metres) and sample fluctuations along the length of the machine, mixing the phases of these fluctuations. Since the floating potential is set by the hotter electron population, the measured Vf fluctuations are no longer related to the local plasma potential fluctuations of a wave by bulk T_e (Carter & Maggs 2009). These primary electrons have a significant effect in the core within the region mapped to the cathode $x \lesssim x_c$. The I_{sat} fluctuations are not affected.
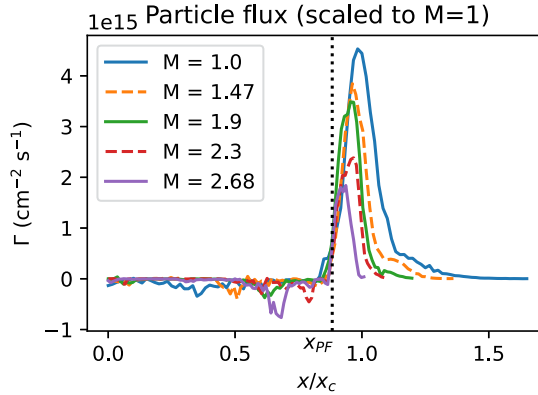
FIGURE 8. Cross-field, $\tilde{E}_y \times B$ fluctuation-based particle flux (calculated using (3.1)) with respect to mirror ratio. A monotonic decrease in particle flux is observed with increasing mirror ratio at the midplane. Particle flux is normalized by plasma circumference to the $M = 1$ case to account for the geometry-induced decrease in particle flux caused by a larger-diameter plasma.

Azimuthal wavenumber is measured by two Vf probe tips 0.5 cm apart. This wavenumber estimation technique yields good agreement with correlation-plane measurements (figure 17). Note that $\tilde{E}$ is not directly measured – it is instead calculated through the $k(\omega)\sqrt{P_{\phi\phi}(\omega)}$ terms.

The $\tilde{E} \times B$ particle flux clearly decreases with mirror ratio; most of this decrease is attributed to the decrease in density fluctuation power. The particle flux for each mirror ratio was normalized to the $M = 1$ case via the plasma circumference to compensate for the increased plasma surface area at the same magnetically mapped coordinate x/x_c. This particle flux is of the order of Bohm diffusion $D_B = \frac{1}{16}T_e/B \approx 6.25$ m^2 s^{-1}, as observed in other transport studies (Maggs, Carter & Taylor 2007).

The T_e profiles and fluctuations may affect particle fluxes but measurements of both were not taken in the same datarun; nevertheless, a quantification of the effect of T_e on particle flux is attempted. The T_e fluctuations affect I_{sat}-based density measurements through the $T_e^{-1/2}$ term, and triple probe and Langmuir sweep T_e measurements suggest that temperature gradients have a negligible impact. A naive incorporation of temperature fluctuation data from DR2 into particle fluxes from DR1 suggests that cross-field particle flux may be underestimated by up to 50 % via the I_{sat} temperature term, but the trend and relative fluxes across mirror ratios remain unchanged. Such a naive incorporation should be treated with suspicion because of the sensitive nature of the flux with respect to the gradient and the differences in profiles between DR1 and DR2. These difference in profiles may be caused by the cathode condition, deposits on the anode or a different gas mix and are difficult to account for.

3.3. *Drift waves*

The I_{sat} fluctuation power spectra in the region of peak power $x \sim x_{PF}$, also where the density gradient is strongest, can be seen in figure 10. Notably, the fluctuation peaks shift to higher frequencies and decrease in total fluctuation power. The shift in frequency may be the Doppler shift caused by the change in $E \times B$ plasma rotation seen in figure 6 at the location $x/x_c \approx x_{PF}$. The shift in frequency is somewhat smaller than what would be expected from the field line-averaged increase in Alfvén speed at the longest possible wavelength. The phase angle of I_{sat} and Vf provides insight into the nature of the driving
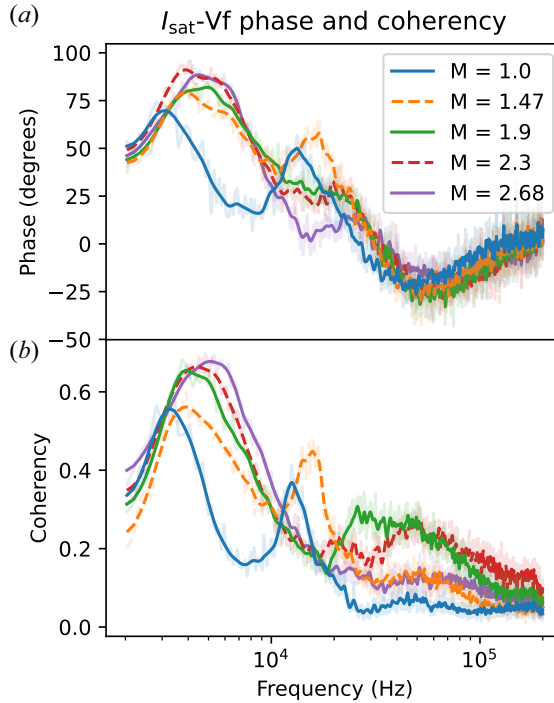
FIGURE 9. Phase (*a*) and coherency (*b*) of I_{sat} current and Vf near x_{PF} at the midplane, smoothed. Positive phase means I_{sat} leads Vf. Peaks in coherency occur between 3 and 5 kHz and at the drift-Alvén wave peaks between 12 and 25 kHz. These coherency peaks tend to have larger phase shifts than other nearby frequencies.

instability. Including a non-zero resistivity η in the drift wave leads to a small phase shift δ between the density and potential. This phase shift δ in a collisional plasmas is of the order of $\delta \approx \omega \nu_e / k_{\parallel}^2 \bar{v}_e^2$ (Horton 1999). Estimating this quantity using measured and typical values ($k_{\parallel} = 0.18$ rad m^{-1}, $\bar{v}_e = 1300$ km s^{-1}, $\nu_e = 3.7$ MHz, $\omega = 12$ kHz) yields a substantial phase shift of $\delta \approx 46°$, which roughly agrees with the phase shifts in figure 9, although the implied increased phase shift at higher frequencies does not agree with measurements.

As seen in figure 9, the phase shift between I_{sat} and Vf fluctuations is larger below 10 kHz, implying the presence of additional modes beyond or significant modification of resistive drift-wave fluctuations. The phase difference between two Vf probes, 3.83 m apart, was used to calculate the parallel wavelength $2\pi / \lambda = k_{\parallel} = \phi_{Vf1, Vf2} / \Delta z$ assuming the wavelengths are greater than 7.66 m. The two probes mapped to the same field line only in the $M = 1$ configuration, so parallel wavenumbers are available only for the flat case. Parallel wavenumbers are theoretically calculable from two-dimensional correlation planes but the coherency dropped dramatically when a mirror geometry was introduced.

A 34 m wavelength mode likely contributes to the measured $k_{\parallel}$ from 3 to $\gtrsim 10$ kHz (figure 11). Drift waves are long-wavelength modes so coherent density and potential fluctuations along the flux tube are expected. The coherency is a measure of similarity of the spectral content of two signals, in this case Vf probes 1 and 2. The coherency is defined as $\gamma = |\langle P_{1,2} \rangle| / \langle |P_{1,1}|^2 \rangle \langle |P_{2,2}|^2 \rangle$, where $P_{x,y}$ is the cross-spectrum between signals x and y and the angle brackets $\langle \rangle$ denote the mean over shots. The coherency between the
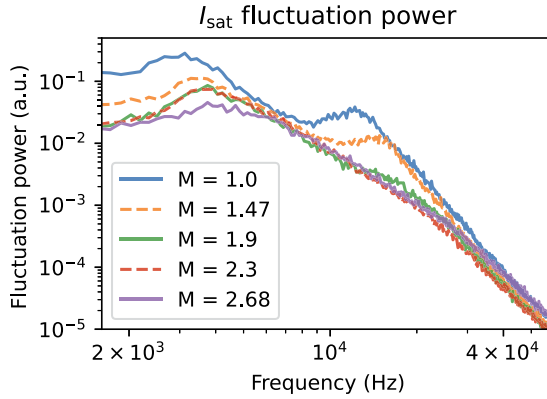
FIGURE 10. The I_{sat} (density) fluctuation power averaged over a 1 cm region around x_{PF} at the midplane. The fluctuation power is largely featureless below 2 kHz and beyond 40 kHz aside from electronics noise.
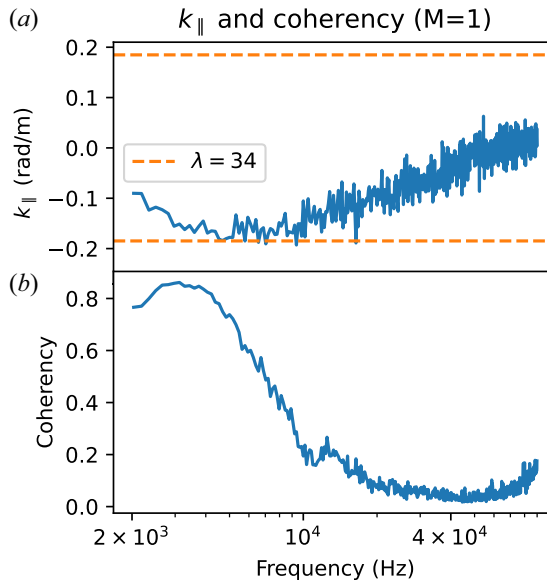

FIGURE 11. Values of $k_\parallel$ (*a*) and coherency γ (*b*) as a function of frequency. Only results from the $M = 1$ case are available, but it is clear that there are long ($\gtrsim$34 m) wavelength modes at 3 and 12 kHz. The probes used for calculating $k_\parallel$ were located at the midplane ($z = 8.31$) and $z = 12.14$ m, 3.83 m apart.

two Vf probes drops off with increasing frequency, with a slight bump at around 12 kHz. There are several candidates for the driving mechanism of the 3–5 kHz mode, but the 12 kHz mode is most likely a drift-Alfvén wave.

3.4. *Turbulence modification*

The wavenumber–power relation in figure 12 shows decreased fluctuation power when a mirror configuration is introduced. However, there is no discernible trend when the mirror ratio is increased further. The exponential nature of the curve also remains unchanged. The greatest decrease in fluctuation power occurred at low and high k_y values, around 10
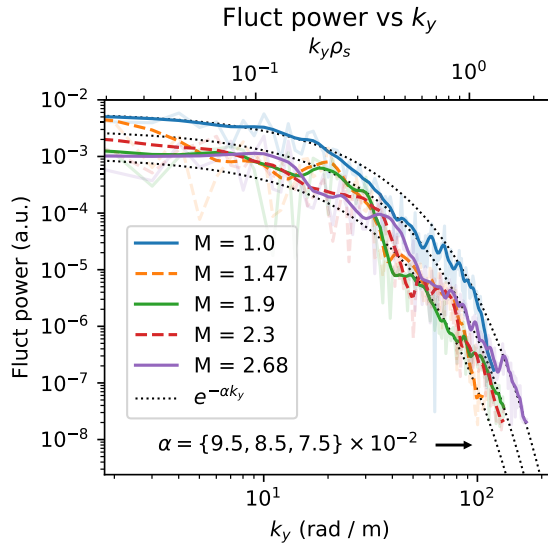
FIGURE 12. Fluctuation power summed for each k_y for frequencies up to 100 kHz, smoothed. The contribution to fluctuation power is negligible past 100 kHz. The fluctuation power decreases substantially when a mirror configuration is introduced, but no trend is seen otherwise and the k_y spectra remain exponential. Note the logarithmic scale.

and 70 rad m^{-1}. The shape of the power-k_y curves follow an exponential distribution, and is inconsistent with a two-dimensional drift-wave turbulent cascade (Wakatani Hasegawa k^{-3}) (Wakatani & Hasegawa 1984). The steep dropoff in fluctuation power with k_y suggests that higher-wavenumber fluctuations do not have a significant effect on transport.

Previous simulations in a flat field (Friedman 2013) predicted frequency and wavenumber spectra that can be fit with many power laws or exponentials, but the data presented here (figures 10, 13, 12) appear to follow an exponential relationship within measurement variation.

Turbulence measurements can be directly compared with theoretical predictions and other devices, as summarized by Liewer (1985). For saturated drift-wave turbulence, one expects the normalized fluctuation level $\tilde{n}/n \sim 1/\langle k_\perp \rangle L_n$, where $k_\perp$ is some typical wavenumber. The power-weighted k_y (calculated from figure 12) was approximately 15 rad m^{-1}, which is an order of magnitude too small to satisfy this relationship. The $\tilde{n}/n$ scaling with ρ_s/L_n, however, is roughly consistent with drift-wave turbulence level saturation: the latter is ≈ 3 times larger. These comparisons suggest that the large, low-frequency fluctuations (~ 3 kHz, which had even smaller k_y) may have a drift-wave turbulence component but are dominantly driven by other instabilities. No trend is seen in ρ_s/L_n and $1/k_y L_n$ when the mirror ratio is varied.

Core fluctuations appear to decrease dramatically, as seen in the I_{sat} fluctuation power (figure 7). The I_{sat} decorrelation time increases from ~ 0.7 ms for $M = 1$ to ~ 2.5 ms for $M = 2.68$. At $x = x_{PF}$, decorrelation times for all mirror ratios remained at 0.2 ms.

3.5. *Magnetic fluctuations*

The perpendicular magnetic fluctuation ($B_\perp$) component of the drift-Alfvén wave can be seen in figure 13. These $B_\perp$ fluctuations are spatially and spectrally coincident with the electrostatic fluctuations (figure 10). Drift-Alfvén waves have been studied in the LAPD in the past (Maggs & Morales 1997; Vincena & Gekelman 2006); strong coupling is
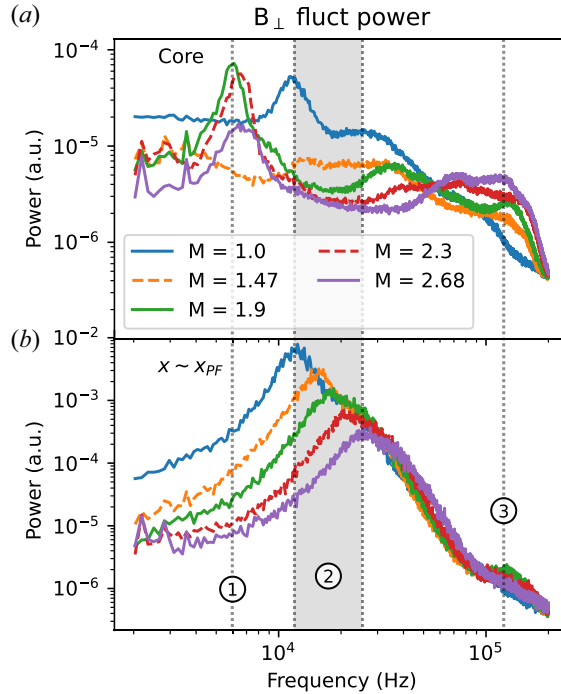
FIGURE 13. The $B_\perp$ fluctuation power averaged at the core from 0 to 3 cm (*a*) and around the peak-fluctuation point ($x \sim x_{PF}$) (*b*). Fluctuation power decreases across the board with mirror ratio except for core frequencies close to Ω_{ci}. Peaks around 10–30 kHz at x_{PF} are consistent (region 2) with drift-Alfvén waves and the near-cyclotron frequency features in the core may be resonating Alfvén waves created by the magnetic mirror. Frequencies below 2 kHz are dominated by instrumentation noise and thus excluded.

observed for $\beta_e > m_e/m_i$ (the electron-ion mass ratio), which is satisfied in this study. The Alfvén speed $\omega/k_\parallel = v_A = B/\sqrt{4\pi n M}$ (given $\omega \ll \Omega_{ci}$) when averaged over the entire column ranges from $\sim$450 to $\sim$1600 km s^{-1}. A $k_\parallel$ corresponding to a wavelength $\lambda = 34$ m roughly falls within the bound established by the kinetic and inertial Alfvén wave dispersion relations at the frequency peaks observed at $x \sim x_{PF}$ seen in figure 13. The lengthening of field lines caused by curvature accounts for at most 10 % of the change in frequency.

The spatial extent of the $B_\perp$ features identified in figure 13 are plotted in figure 14. Feature 1 at $\approx$6 kHz shows increased fluctuation amplitudes at $x = 0$ for mirror ratios 1.9 and above, but for $M = 1$ and $M = 1.47$ there is no increase in fluctuation power. A similar feature, but at a much smaller level, is observed in the I_{sat} fluctuation power in the core as well. This core feature may be caused by the hole in the core seen in the I_{sat} profile (figure 3) driving low-amplitude waves or instabilities. Feature 2 in figure 14 is the magnetic component of the drift-Alfvén wave. The fluctuation power peaks at the gradient region and corresponds with the peak in density fluctuations (figure 7).

Feature 3 is particularly interesting because this the only fluctuating quantity to increase with mirror ratio, seen in figure 15. This feature may be broad evanescent Alfvénic fluctuations from the plasma source. These fluctuations have been observed in the LAPD in the source region alongside an Alfvén wave maser (Maggs, Morales & Carter 2005). Note that the Alfvén maser cannot enter the mirror cell at mirror ratios greater than 1.75 because the Alfvén maser resonates at $0.57 f_{ci}$ but the midplane is always at or near 500 G.
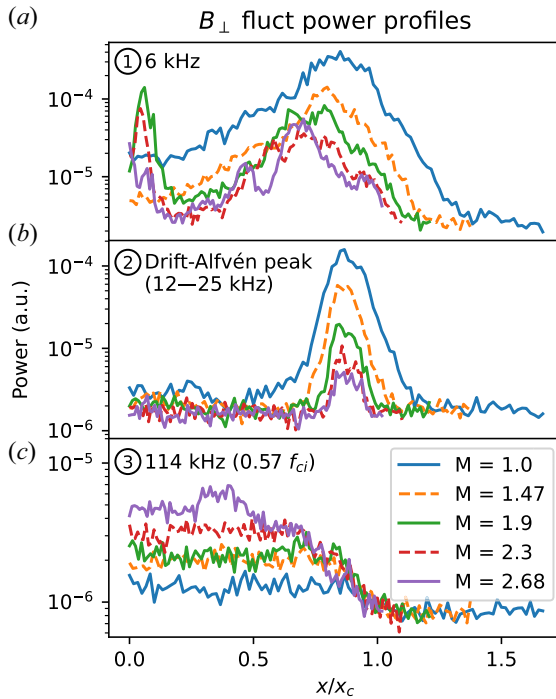
FIGURE 14. The $B_\perp$ fluctuation power profiles for the three regions shown in figure 13: region 1 (6 kHz) (*a*), region 2, where frequencies are taken from the peaks of the drift-Alfvén waves for each mirror ratio, (*b*) and region 3 (114 kHz) (*c*).
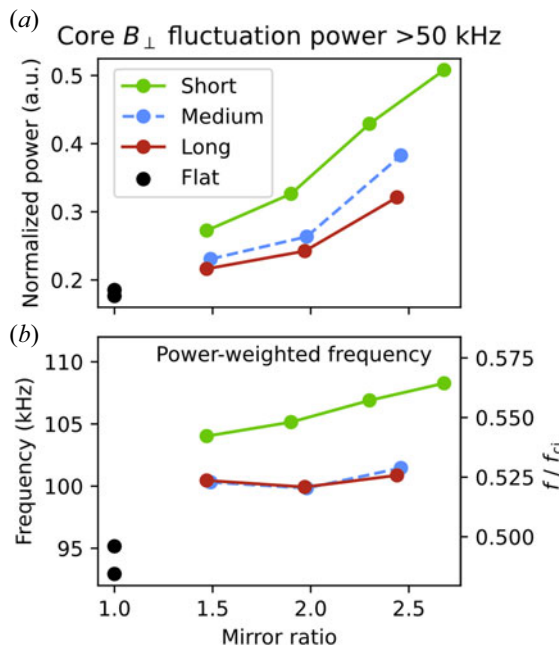

FIGURE 15. Summed fluctuation power of $B_\perp$ in the core ($x/x_c \leqslant 0.3$) as a function of mirror length and ratio. (*a*) The fluctuation power is normalized by the sum of the full-spectrum summed power. (*b*) The frequency of the power distribution >50 kHz weighted by the fluctuation power.
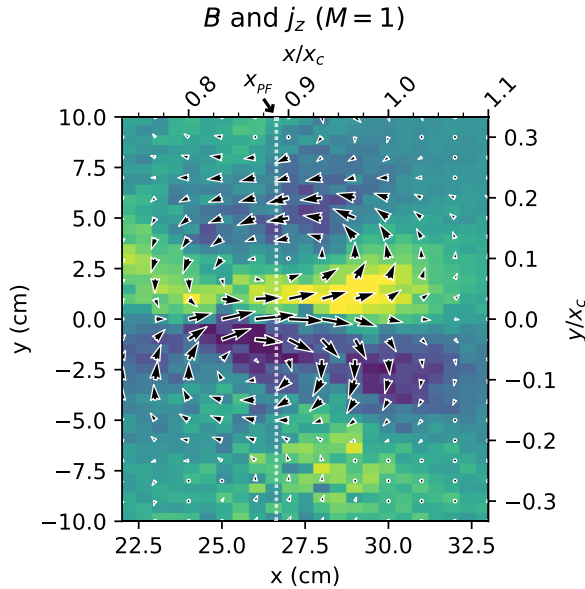
FIGURE 16. Perpendicular magnetic field and the derived current density for the flat-field ($M = 1$) case using a Bdot probe with an axially separated I_{sat} reference (DR2). The x–y plane was centred near x_{PF}.

The sub-2 kHz modes in $B_\perp$ and the harmonics of these modes are nearly constant in power across the entire plasma; these features are likely perturbations from the magnet power supplies and thus ignored. The lack of radial, azimuthal and axial structure in these magnetic signals below 2 kHz and narrow bandwidth indicate a non-plasma origin. Significant radial and azimuthal structure in $B_\perp$ fluctuation power starts to appear in frequencies larger than 4 kHz.

4. Two-dimensional structure

The perpendicular magnetic field structure is measured by collecting x–y planar Bdot ($dB_{\{x,y,z\}}/dt$) data alongside a stationary, axially separated I_{sat} reference probe (DR2). This probe provides a phase reference for the magnetic field fluctuations, allowing a two-dimensional map of relative phase to be constructed over many shots. Only the region around x_{PF} was measured because of constraints on probe movement. The amplitude and phases for each magnetic field component are then used to reconstruct the local magnetic fluctuation vector $\boldsymbol{B}$. The axial current density structure, j_z, can be derived from this vector field. $\boldsymbol{B}$ and the corresponding j_z for the flat-field ($M = 1$) case can be seen in figure 16. Two main current channels can be seen with the magnetic fields circulating around them. This structure quickly decoheres in time as expected in a turbulent plasma. At higher mirror ratios, the field magnitude and corresponding current density decrease (which was also seen in DR1: figure 13).

Using two, axially separated, correlated I_{sat} measurements (DR2), with one collecting x–y planar data, the azimuthal mode number m (radially integrated) was calculated. Higher-frequency and higher-m features are seen with increasing mirror ratio (figure 17). The increased frequencies may be caused by a change in Doppler shift by the $\boldsymbol{E} \times \boldsymbol{B}$ flow. This higher-m trend suggests that azimuthal structures do not scale with increased plasma radius but instead remain roughly the same size. The limited planar probe movement
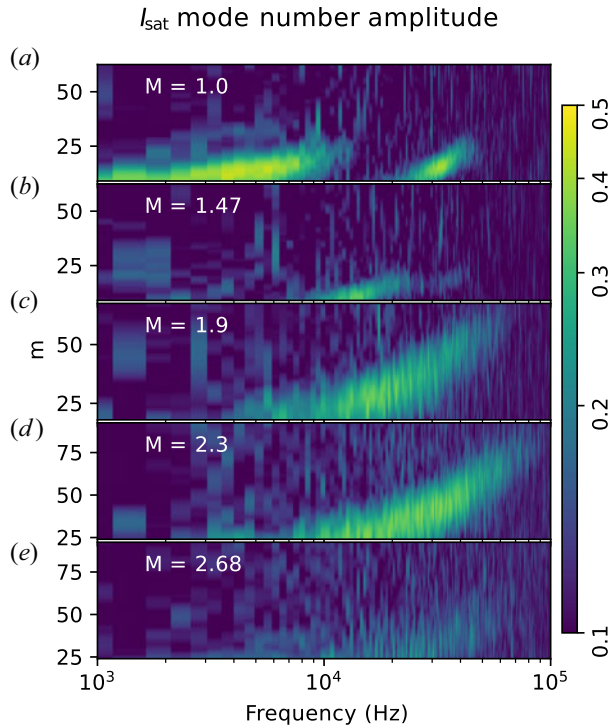
FIGURE 17. Azimuthal mode number m amplitudes calculated from two axially separated, correlated, I_{sat} probes. Increasing mirror ratio (*a–e*) leads to increased m at higher frequencies. (DR2).

caused an increase in the lower bound on m at higher mirror ratios. At mirror ratios 1.47 and higher, the lower-frequency component (<10 kHz) appears to decrease significantly in amplitude. Calculating $k_\perp$ from m evaluated at $x \sim x_c$ yields similar k_y values as the two-tip technique (figure 18). The average k_y for a given frequency can be calculated using two Vf tips on the same probe by calculating the phase difference and dividing by the spatial separation of 5 mm: $k_y = \phi_{\text{vf1,vf2}}/\Delta y$ (Beall, Kim & Powers 1982). The maximum $|k_y|$ measurable before aliasing is $\pi/\Delta y \approx 628$ rad m^{-1}. As seen in figure 18, the k_y spectrum remains similar across mirror ratios, but the wavenumber extends further into higher frequencies with increasing mirror ratio. These azimuthal mode numbers and gradient scale lengths are consistent with linear simulations using the three-dimensional fluid code BOUT (Popovich *et al.* 2010) in the flat, unbiased case.

5. Discussion

5.1. *Lack of mirror-driven instabilities*

No evidence is seen for mirror-driven instabilities – curvature, loss cone or otherwise. Given the LAPD parameters in this study (tables 1 and 2), the collision frequencies are sufficiently high such that the mirror is in the gas-dynamic regime: losses out of the mirror throat are governed by gas-dynamic equations rather than free streaming through the loss cone. To be in the gas-dynamic regime, the mirror length must exceed the mean free path of the ions (Ivanov & Prikhodko 2013)

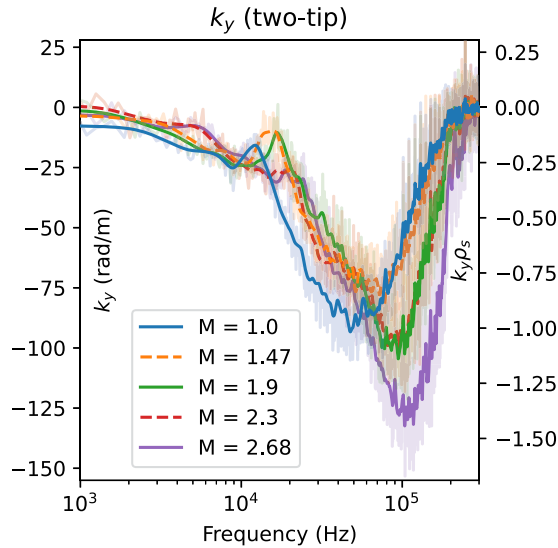$$L > \lambda_{\text{ii}} \ln M/M, \tag{5.1}$$

FIGURE 18. The value of k_y averaged about x_{PF} and smoothed for each mirror ratio calculated using two vertically separated Vf tips on the same probe. Little change is seen in k_y at lower frequencies but higher frequencies tend towards larger k_y at higher mirror ratios.

where L is the mirror length, λ_{ii} is the ion mean free path and M is the mirror ratio. These collisions populate the loss cone and maintain a (cold) Maxwellian distribution, eliminating the possibility of loss-cone-, ion-driven instabilities like the Alfvén-ion cyclotron (AIC) (Casper & Smith 1982) or drift-cyclotron loss-cone (DCLC) (Simonen 1976; Kanaev 1979) instabilities that have been observed in other (historic) devices.

The paraxial, approximate interchange growth rate is (Post 1987; Ryutov *et al.* 2011)

$$\Gamma_0 = \frac{c_s}{\sqrt{L_M L_P}}, \tag{5.2}$$

which yields $\Gamma_0 \approx 1.2$ kHz using $L_M \approx 7$ m and $L_P = 17$ m. Here, c_s is used instead of $\overline{v_i}$ because $T_i \ll T_e$ and the mirror length L is split to distinguish between the contributions of the plasma length and mirror length to inertia and to curvature drive, respectively. Interchange is not visible, in part because the aspect ratio of these mirrors is quite large, limiting the growth rate of interchange. The length of the mirror (3.5 m), radius of curvature (6–7 m) and plasma column (17 m) are much larger than the radius of the plasma (0.5 m maximum), so the plasma inertia is large relative to the instability drivers. Line tying to the cathode may further lower the growth rate. The hot cathode used for plasma formation could function as a thermionic endplate that can supply current to short out the flute-like interchange perturbations. Line tying has been seen in flux rope experiments on the LAPD using a hotter, denser source (Van Compernolle *et al.* 2011), also in other devices (Fornaca, Kiwamoto & Rynn 1979), and is why interchange was not seen in the earliest mirror machines (Post 1987). Note that the plasma terminates on the cathode or end plates before the magnetic field flares out, so there is no contribution to stability from an expander tank as seen in other GDTs (Ryutov *et al.* 2011; Ivanov & Prikhodko 2013). Finite Larmor radius (FLR) effects may provide a stabilizing effect for larger azimuthal mode numbers. At the highest mirror ratio, assuming a plasma radius of $a_0 = \sqrt{2.68} * x_{PF} = 43$ cm, the FLR stability criterion $(m/2)(\rho_i L/a_0^2) > 1$ (Ryutov *et al.* 2011) suggests a stabilizing effect may be present for azimuthal mode numbers $m > 4$.

If the curvature-induced interchange instability were observable, then introducing a mirror configuration would lead to new features in I_{sat} and Bdot fluctuations. In particular, low-frequency mode(s) – likely less than 10 kHz given the low m number and plasma rotation rates – would be observed growing from the pressure gradient region. For onset of the interchange instability, the mirror curvature or plasma pressure would need to be increased but the precise conditions required for this onset are not yet known for the LAPD.

Interchange could also be at least partially stabilized by the continuous production of electrons in the core that are electrostatically trapped by the ambipolar potential (Guest & Harris 1971). The intuition behind this stabilization mechanism is as follows: electrons are continuously produced via ionization of neutrals, and any change in the local potential will cause more or fewer electrons to be lost out the ends of the device along that field line, counteracting the potential change. This stabilization mechanism has been experimentally demonstrated to completely suppress interchange when the ambipolar potential $\Phi \gtrsim 6T_e$ (Komori *et al.* 1987).

The $E \times B$ shear flow present (figure 6) may also make a contribution to the stabilization of interchange (Bagryansky *et al.* 2003, 2007; Beklemishev *et al.* 2010; Ryutov *et al.* 2011). The estimated shearing rate is between 3 and 10 kHz, which is greater than the estimated ≈ 1.2 kHz growth rate of the interchange mode.

5.2. *Instabilities driving turbulence*

Rotational interchange can be significant driver of the broadband turbulence spectrum in the LAPD, particularly when a biased limiter is installed. This observation has been confirmed by both linear simulations (Popovich *et al.* 2010) and biasing experiments (Schaffner 2013).

This rotational interchange mode has the following attributes, as summarized by Jassby (1972): flute-like ($k_\parallel = 0$), $|e\tilde{\phi}/T_e|/|\tilde{n}/n| \gtrsim 1$, radial potential phase variation 45 to 90°, maximum possible $|e\tilde{\phi}/T_e| < 1$. All of these attributes are seen for the lower-frequency (3 kHz) mode. The Vf radial phase variation when $M > 1$ is not clearly seen because the coherency is dramatically reduced along the field line. The rotational interchange mode could couple with the drift wave at $k_\parallel = \pi/L \sim 0.37$ rad m^{-1} ($n = 0.5$), which has been observed in the past (Schaffner 2013) and likely present here. Estimates of shearing rate from the $E \times B$ flow velocity profile (figure 6), calculated fluctuation ratios and radial phase shift variation suggest that Kelvin–Helmholtz-driven turbulence is not significant, if present at all. Historically, biasing a limiter has been required to clearly observe the Kelvin–Helmholtz instability (Horton *et al.* 2005; Schaffner *et al.* 2012; Schaffner 2013).

Low-frequency density fluctuations may also be driven by a flute-like conducting-wall temperature-gradient instability which only requires an electron temperature gradient to grow (even with straight field lines) (Berk, Ryutov & Tsidulko 1991). Simulations of turbulence in the LAPD suggest the possible presence of these conducting-wall modes (CWMs) which have the highest growth rate for $m \leqslant 20$ (Friedman *et al.* 2013). This lower-m mode could be responsible for the peak around 3 kHz in the $M = 1$ I_{sat} fluctuation (figure 10) and azimuthal mode numbers (figure 17) and for the low-frequency low-$k_\parallel$ or flute-like behaviour (figure 11). This CWM may also be responsible for flatter electron temperature profiles seen in previous studies (Schaffner 2013; Perks *et al.* 2022) (figure 5).

These linearly unstable modes may be outgrown by a rapidly growing nonlinear instability that couples to drift-like modes, as suggested by simulations (Friedman *et al.* 2013). This nonlinear instability is driven by the density gradient at an axial mode number of $n = 0$ and nonlinearly transfers energy to $n \neq 0$ fluctuations.
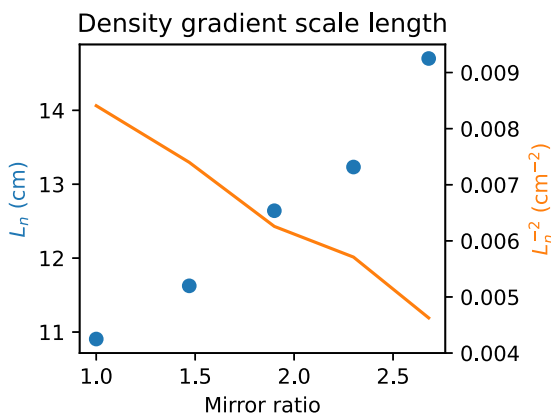
FIGURE 19. Gradient scale length L_n and the associated term in the drift-wave growth rate L_n^{-2}. This scale length was calculated over a 3 cm region around x_{PF} (peak-fluctuation region) at the midplane. Increasing the mirror ratio increases the gradient scale length, which suggests weakening of the underlying instability driver.

The CWM and nonlinear instability may be present in these mirror experiments but the spectra are adequately explained by linearly unstable modes. Precise identification these modes requires further study; neither of these instabilities have been directly observed in the LAPD.

5.3. *Causes of particle flux reduction*

The reduction in particle flux explained by a reduction in density fluctuations likely caused by a increased gradient scale length $L_n = n/\nabla n$ (figure 19), decreasing the linear drift-wave growth rate and saturation level seen in § 3.4. This gradient length reduction may also reduce the growth rate of the rotational interchange instability, which may be the dominate driver for the low-frequency large-amplitude density fluctuations.

The decorrelation time of I_{sat} time series data is around 0.15 ms at x_{PF}. An estimate of the $E \times B$ flow shear from figure 6 (DR2) yields a shearing time between 0.1 and 0.3 ms at x_{PF}. These times suggest that spontaneous flow shear may be important for suppressing turbulence, as seen in other studies (Cho *et al.* 2005; Schaffner *et al.* 2013), at all mirror ratios. However, no clear trend in shearing strength is seen with mirror ratio.

It is important to note that the electron thermal diffusion time along the field line is very long compared with the frequency of the drift wave ($\omega \gtrsim k_\parallel \bar{v}_e^2/\nu_{ei}$) (Goldston 1995) so the electron temperature along the field line may not be constant on the drift-wave time scale. This factor is not taken into account in this analysis but may have substantial impact on interpretations of the measured phase shift.

6. Conclusions and future work

Turbulence and transport were studied in mirrors with varying lengths and ratios using the flexible magnetic geometry of the LAPD. Particle flux and fluctuation amplitudes decreased up to a factor of two when the mirror ratio was increased. The primary drivers of turbulence were identified as the rotational interchange mode, caused by spontaneous rotation, and unstable drift-Alfvén waves driven by the density gradient. The decrease in density fluctuation amplitudes can be attributed to an increase in the gradient scale length caused by the dimensionally wider plasma at the mirror midplane. Despite imposing a mirror configuration, no signs of mirror-driven instabilities were observed. The highly

collisional, GDT-like plasma produced suppressed any velocity space instabilities. The interchange growth rate was likely suppressed to an undetectable level by line tying, in-cell electron production and shear flow.

Future experiments in hotter regimes with the new LaB6 cathode (Qian *et al.* 2023) will need to be performed to evaluate the robustness of these results, particularly concerning the stabilization of curvature-induced interchange. Additionally, the source field should be matched to the mirror midplane field so that the plasma remains at the same radius to isolate geometric effects. Simultaneous measurements using flux and/or vorticity probes and I_{sat} are needed to concretely determine if azimuthal flow shear is modified by the mirror field, and to quantify the effect of flows on rotational interchange and drift-wave instability drive in general. Multiple simultaneous axial measurements of potential would enable better understanding of the axial wavenumber and identification of possible modes.

Acknowledgements

Funding

Declaration of interests

The authors report no conflict of interest.

Data availability

The data and code supporting this study are available from the corresponding author upon reasonable request.

REFERENCES

BAGRYANSKY, P.A., BEKLEMISHEV, A.D. & SOLDATKINA, E.I. 2007 Influence of radial electric field on high-beta plasma confinement in the gas dynamic trap. *Fusion Sci. Technol.* **51** (2T), 340–342.

BAGRYANSKY, P.A., LIZUNOV, A.A., ZUEV, A.A., KOLESNIKOV, E.YU. & SOLOMACHIN, A.L. 2003 Experiments with controllable application of radial electric fields in GDT central cell. *Fusion Sci. Technol.* **43** (1T), 152–156.

BEALL, J.M., KIM, Y.C. & POWERS, E.J. 1982 Estimation of wavenumber and frequency spectra using fixed probe pairs. *J. Appl. Phys.* **53** (6), 3933–3940.

BEKLEMISHEV, A.D., BAGRYANSKY, P.A., CHASCHIN, M.S. & SOLDATKINA, E.I. 2010 Vortex confinement of plasmas in symmetric mirror traps. *Fusion Sci. Technol.* **57** (4), 351–360.

BERK, H.L., RYUTOV, D.D. & TSIDULKO, YU.A. 1991 Temperature-gradient instability induced by conducting end walls. *Phys. Fluids* B **3** (6), 1346–1354.

BROCHARD, F., GRAVIER, E. & BONHOMME, G. 2005 Transition from flute modes to drift waves in a magnetized plasma column. *Phys. Plasmas* **12** (6), 062104.

CARTER, T.A. & MAGGS, J.E. 2009 Modifications of turbulence and turbulent transport associated with a bias-induced confinement transition in the Large Plasma Device. *Phys. Plasmas* **16** (1), 012304.

CASPER, T.A. & SMITH, G.R. 1982 Observation of alfvén ion-cyclotron fluctuations in the end-cell plasma in the tandem mirror experiment. *Phys. Rev. Lett.* **48**, 1015–1018.

CHO, T., *et al.* 2005 Observation of the effects of radially sheared electric fields on the suppression of turbulent vortex structures and the associated transverse loss in GAMMA 10. *Phys. Rev. Lett.* **94** (8), 085002.

ENDRIZZI, D., *et al.* 2023 Physics basis for the Wisconsin HTS Axisymmetric Mirror (WHAM). *J. Plasma Phys*. **89** (5), 975890501.

EVERSON, E.T., PRIBYL, P., CONSTANTIN, C.G., ZYLSTRA, A., SCHAEFFER, D., KUGLAND, N.L. & NIEMANN, C. 2009 Design, construction, and calibration of a three-axis, high-frequency magnetic probe (B-dot probe) as a diagnostic for exploding plasmas. *Rev. Sci. Instrum*. **80** (11), 113505.

FASOLI, A., LABIT, B., MCGRATH, M., MÜLLER, S.H., PLYUSHCHEV, G., PODESTÀ, M. & POLI, F.M. 2006 Electrostatic turbulence and transport in a simple magnetized plasma. *Phys. Plasmas* **13** (5), 055902.

FERRON, J.R., WONG, A.Y., DIMONTE, G. & LEIKIND, B.J. 1983 Interchange stability of an axisymmetric, average minimum-*B* magnetic mirror. *Phys. Fluids* **26** (8), 2227–2233.

FOREST, C.B., *et al.* 2024 Prospects for a high-field, compact break-even axisymmetric mirror (BEAM) and applications. *J. Plasma Phys*. **90** (1), 975900101.

FORNACA, S., KIWAMOTO, Y. & RYNN, N. 1979 Experimental stabilization of interchange mode by surface line tying. *Phys. Rev. Lett*. **42**, 772–776.

FRIEDMAN, B.C. 2013 Simulation analysis of zero mean flow edge turbulence in LAPD. PhD thesis. University of California, Los Angeles.

FRIEDMAN, B., CARTER, T.A., UMANSKY, M.V., SCHAFFNER, D. & JOSEPH, I. 2013 Nonlinear instability in simulations of Large Plasma Device turbulence. *Phys. Plasmas* **20** (5), 055704.

GEKELMAN, W., *et al.* 2016 The upgraded Large Plasma Device, a machine for studying frontier basic plasma physics. *Rev. Sci. Instrum*. **87** (2), 025105.

GOLDSTON, R.J. 1995 *Introduction to Plasma Physics*. CRC.

GUEST, G.E. & HARRIS, E.G. 1971 Flute stabilization via electrostatically confined cold electrons. *Phys. Rev. Lett*. **27**, 1500–1503.

HOOPER, E.B. JR., BALDWIN, D.E., FOWLER, T.K., KANE, R.J. & TURNER, W.C. 1984 Radial transport reduction in tandem mirrors using end-wall boundary conditions. *Phys. Fluids* **27** (9), 2264–2267.

HORTON, W. 1999 Drift waves and transport. *Rev. Mod. Phys*. **71** (3), 735–778.

HORTON, W., PEREZ, J.C., CARTER, T. & BENGTSON, R. 2005 Vorticity probes and the characterization of vortices in the Kelvin–Helmholtz instability in the large plasma device experiment. *Phys. Plasmas* **12** (2), 022303.

IVANOV, A.A. & PRIKHODKO, V.V. 2013 Gas-dynamic trap: an overview of the concept and experimental results. *Plasma Phys. Control. Fusion* **55** (6), 063001.

JASSBY, D.L. 1972 Transverse velocity shear instabilities within a magnetically confined plasma. *Phys. Fluids* **15** (9), 1590–1604.

KANAEV, B.I. 1979 Stabilization of drift loss-cone instability (DCI) by addition of cold ions. *Nucl. Fusion* **19** (3), 347.

KOMORI, A., HIGUCHI, Y., SUETSUGU, Y., YONESU, A. & KAWAI, Y. 1987 Flute stabilization of a mirror-confined plasma by a positive ambipolar potential. *J. Phys. Soc. Japan* **56** (8), 2607–2610.

LIEWER, P.C. 1985 Measurements of microturbulence in tokamaks and comparisons with theories of turbulence and anomalous transport. *Nucl. Fusion* **25** (5), 543–621.

MAGGS, J.E., CARTER, T.A. & TAYLOR, R.J. 2007 Transition from Bohm to classical diffusion due to edge rotation of a cylindrical plasma. *Phys. Plasmas* **14** (5), 052507.

MAGGS, J.E. & MORALES, G.J. 1997 Fluctuations associated with a filamentary density depletion. *Phys. Plasmas* **4** (2), 290–299.

MAGGS, J.E., MORALES, G.J. & CARTER, T.A. 2005 An Alfvén wave maser in the laboratory. *Phys. Plasmas* **12** (1), 013103.

MASE, A., ITAKURA, A., INUTAKE, M., ISHII, K., JEONG, J.H., HATTORI, K. & MIYOSHI, S. 1991 Control of the radial electric field and of turbulent fluctuations in a tandem mirror plasma. *Nucl. Fusion* **31** (9), 1725.

PERKS, C., MORDIJCK, S., CARTER, T., VAN COMPERNOLLE, B., VINCENA, S., ROSSI, G. & SCHAFFNER, D. 2022 Impact of the electron density and temperature gradient on drift-wave turbulence in the Large Plasma Device. *J. Plasma Phys*. **88** (4), 905880405.

POLI, F.M., BRUNNER, S., DIALLO, A., FASOLI, A., FURNO, I., LABIT, B., MÜLLER, S.H., PLYUSHCHEV, G. & PODESTÀ, M. 2006 Experimental characterization of drift-interchange instabilities in a simple toroidal plasma. *Phys. Plasmas* **13** (10), 102104.

POPOVICH, P., UMANSKY, M.V., CARTER, T.A. & FRIEDMAN, B. 2010 Analysis of plasma instabilities and verification of the BOUT code for the Large Plasma Device. *Phys. Plasmas* **17** (10), 102107.

POST, R.F. 1987 The magnetic mirror approach to fusion. *Nucl. Fusion* **27** (10), 1579.

POWERS, E.J. 1974 Spectral techniques for experimental investigation of plasma diffusion due to polychromatic fluctuations. *Nucl. Fusion* **14** (5), 749.

QIAN, Y., *et al.* 2023 Design of the Lanthanum hexaboride based plasma source for the large plasma device at UCLA. *Rev. Sci. Instrum.* **94** (8), 085104.

RYUTOV, D.D., BERK, H.L., COHEN, B.I., MOLVIK, A.W. & SIMONEN, T.C. 2011 Magneto-hydrodynamically stable axisymmetric mirrors. *Phys. Plasmas* **18** (9), 092301.

SCHAFFNER, D. 2013 Study of flow, turbulence and transport on the large plasma device. PhD thesis. University of California, Los Angeles.

SCHAFFNER, D.A., CARTER, T.A, ROSSI, G.D., GUICE, D.S., MAGGS, J.E., VINCENA, S. & FRIEDMAN, B. 2012 Modification of turbulent transport with continuous variation of flow shear in the Large Plasma Device. *Phys. Rev. Lett.* **109** (13), 135002.

SCHAFFNER, D.A., CARTER, T.A., ROSSI, G.D., GUICE, D.S., MAGGS, J.E., VINCENA, S. & FRIEDMAN, B. 2013 Turbulence and transport suppression scaling with flow shear on the Large Plasma Device. *Phys. Plasmas* **20** (5), 055907.

SIMONEN, T.C. 1976 Measurements of ion cyclotron instability characteristics in a mirror-confined plasma. *Phys. Fluids* **19** (9), 1365–1370.

TYNAN, G.R., FUJISAWA, A. & MCKEE, G. 2009 A review of experimental drift turbulence studies. *Plasma Phys. Control. Fusion* **51** (11), 113001.

VAN COMPERNOLLE, B., GEKELMAN, W., PRIBYL, P. & COOPER, C.M. 2011 Wave and transport studies utilizing dense plasma filaments generated with a lanthanum hexaboride cathode. *Phys. Plasmas* **18** (12), 123501.

VINCENA, S. & GEKELMAN, W. 2006 Drift-Alfvén wave mediated particle transport in an elongated density depression. *Phys. Plasmas* **13** (6), 064503.

WAKATANI, M. & HASEGAWA, A. 1984 A collisional drift wave description of plasma edge turbulence. *Phys. Fluids* **27** (3), 611–618.

WICKHAM, M. & VANDEGRIFT, G. 1982 Curvature-induced interchange mode in an axisymmetric plasma. *Phys. Fluids* **25** (1), 52–58.

YOSHIKAWA, M., *et al.* 2010 Use of a gold neutral beam probe to study fluctuation suppression during potential formation in the GAMMA 10 tandem mirror. *Fusion Sci. Technol.* **57** (4), 312–319.